

UCLA

Adaptive Optics for Extremely Large Telescopes 4 - Conference Proceedings

Title

Low Wind Effect, the main limitation of the SPHERE instrument

Permalink

<https://escholarship.org/uc/item/910646qf>

Journal

Adaptive Optics for Extremely Large Telescopes 4 - Conference Proceedings, 1(1)

Authors

Sauvage, Jean-François

Fusco, Thierry

Guesalaga, Andres

et al.

Publication Date

2015

DOI

10.20353/K3T4CP1131541

Copyright Information

Copyright 2015 by the author(s). All rights reserved unless otherwise indicated. Contact the author(s) for any necessary permissions. Learn more at

<https://escholarship.org/terms>

Peer reviewed

Low Wind Effect, the main limitation of the SPHERE instrument

Sauvage Jean-François,^{a,b} Fusco Thierry,^{a,b} Guesalaga Andres,^{c,b,d} Wizinowitch Peter,^c O'Neal Jared,^f N'Diaye Mamadou,^g Vigan Arthur,^b Girard Julien,^f Lesur Geoffroy,^h Mouillet David,^h Beuzit Jean-Luc,^h Kasper Markus,^f Le Louarn Miska,^f Milli Julien,^f Dohlen Kjetil,^b Neichel Benoît,^b Bourget Pierre,^f Heigenauer Pierre,^f Mawet Dimitriⁱ

^a ONERA - Optics Department, 29 avenue de la Division Leclerc, F-92322 Chatillon Cedex, France

^b Aix Marseille Universite, CNRS, LAM (Laboratoire d'Astrophysique de Marseille) UMR 7326, 13388, Marseille, France

^c Department of Electrical Engineering, School of Engineering, Pontificia Universidad Católica de Chile

^d Fondation IMéRA (L'institut d'études avancées d'Aix-Marseille) 2, Place Le Verrier 13004 Marseille-FranceIMERA,

^e W. M. Keck Observatory, 65-1120 Mamalahoa Hwy, Kamuela, HI, USA 96743

^f ESO European Southern Observatory, Karl-Schwarzschild-Strasse 2, D-85748 Garching

^g STScI Space Telescope Science Institute, Baltimore

^h IPAG UJF-Grenoble 1 / CNRS-INSU, Institut de Planétologie et d'Astrophysique de Grenoble (IPAG) UMR 5274, Grenoble, F-38041, France

ⁱ JPL, Pasadena

ABSTRACT

The SPHERE instrument (Beuzit, et al., 2010) is dedicated to the direct imaging of extra-solar planets. This kind of observation allows one to study the photons emitted by the planet's atmosphere itself, or reflected by its surface. The search for bio-markers is therefore made possible. The SPHERE instrument has been installed and commissioned at VLT Paranal Observatory during 2014 and now routinely delivers high contrast images to the exoplanet community. This paper presents a study of the main actual limitation of the SPHERE instrument, as known as the Low Wind Effect [LWE]. This effect has been discovered on SPHERE during commissioning period. Its effect is a strong degradation of the instrument PSF, preventing instrument to perform high contrast imaging. It happens during particularly low wind conditions (below 1m/s at the telescope level) which happens one night out of five.

Keywords: extreme adaptive optics, high contrast imaging, dome seeing.

1. INTRODUCTION

The direct imaging of extra-solar planets is one of the most exciting challenges of today's astronomy. From a scientific point-of-view, the light coming from an extra-solar planet is able to reveal the chemical elements of its atmosphere. Direct imaging of exoplanets therefore enables in a short term the search for habitable planets and eventually extraterrestrial life. The year 2014 has seen a real revolution with the delivery of an instruments fully dedicated to high contrast, and opened to a wide community: SPHERE (Spectro Polarimetric High contrast Exoplanet REsearch) is one of them. It already began to provide lots of science results (Vigan, et al., 2015) (Mesa, et al., 2015) (Zurlo, et al., 2014).

The installation of SPHERE at VLT required four periods of intense commissioning. The overall performance, operation and maintenance of the numerous observing modes of the instrument has been thoroughly studied and assessed. The eXtreme Adaptive Optics [XAO] system SAXO (Fusco, et al., 2006; Fusco, et al., 2014) has been tested and its performance have been measured for a whole range of atmospheric conditions and guide star magnitude. The three instrument (Infrared camera IRDIS, Integral field spectrograph IFS and visible polarimetric imager ZIMPOL) have demonstrated the highest expected detectivity level.

The commissioning periods, as well as the Science Verification Time [SVT] allowed one to make a full use of the performance of the instrument and already produce a lot of high quality science innovations. During these periods, an effect called “Low Wind Effect” has been diagnosed on SPHERE. This effect has been linked to the thematic of Dome seeing effects, which is a research field that always accompanied the astronomical observations (Woolf, 1979). In section 2, the discovery of the low wind effect is detailed. A first understanding of the effect is proposed in the section 3. The inspection of Adaptive optics data is proposed in section 4. Then a scenario explaining the LWE is described in section 5. In section 6, a criterion is defined so as to bring a first solution to LWE quantification during the science observation. In last section 7, the perspectives of how to deal with such an effect with the AO system are listed.

2. DISCOVERY OF LOW WIND EFFECT

The Low Wind Effect [LWE] characterizes an effect, discovered during the first commissioning in May 2014. The effect has been seen by all the imagers of SPHERE, in the same way. I will only use H band images from the Differential Tip-Tilt Sensor [DTTS] of SPHERE. This H band imager is situated in a focal plane, as close as possible to the IR coronagraphic plane. The instrument Point Spread Function [PSF] measured on-sky by the DTTS, simply by imaging a single star, degrades from to Figure 1 (a) to Figure 1 (b). The first and circular Airy ring is degraded into several pieces, and the Strehl Ratio [SR] is strongly degraded. The star light, as seen in Figure 1 (b), presents residual speckles that will generate bright spots in the coronagraphic image, close to optical axis. According to the PSF development for small aberrations of Perrin et al 2003, these bright speckles are pinned to the first Airy ring. The imaging quality does not allow anymore to provide high contrast capacities. Moreover, the shape of the PSF evolves slowly with time, creating artefacts in the Angular Differential Imaging [ADI] capacities of the instrument. This observing mode is therefore the most impacted by the LWE on SPHERE.

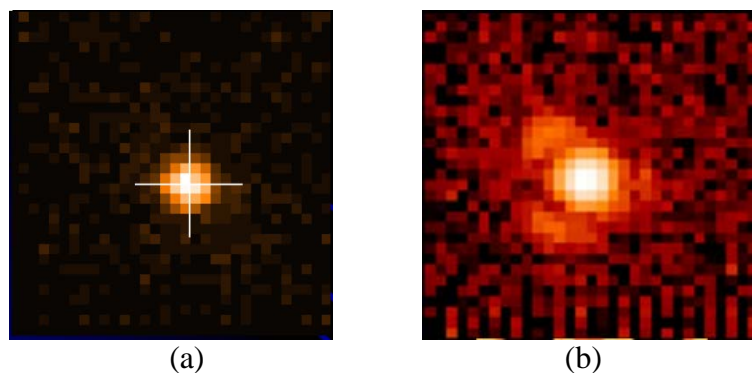


Figure 1: PSF of SPHERE instrument in H band, as seen by the DTTS. (a) in absence of LWE. (b) in presence of LWE.

The LWE can take many shapes, as shown in Figure 2. A small version of the LWE is shown in (a) where a single additional speckle is visible on top/left side of the central PSF. Intermediate version of LWE are shown in (b) and (c) where two to three additional bright spots are visible. The strongest version of the effect is shown on (d) where four spots are visible, and the main central core is no more discernable.

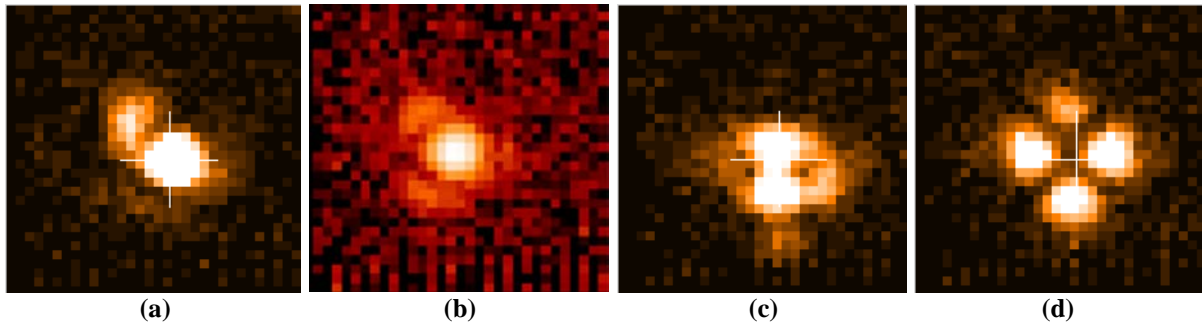


Figure 2 : Different amplitudes for the LWE, from a small effect (a) to a large effect (d). The time, as well as the guide star magnitude varies from (a) to (d), explaining the apparent variation of flux.

Thanks to the systematic measurement of the wind speed in the telescope unit, a strong correlation has been made between the LWE and the wind speed. As illustrated on Figure 3, the phenomenon appears systematically when the wind speed at the secondary level drops below 1m/s. The effect is known to last as long as the wind speed remains below this limit. During the night of August, 8th, the wind speed remained below 1m/s during whole night, no science observation could be made. As soon as the wind speed increases above 1m/s, the effect disappears.

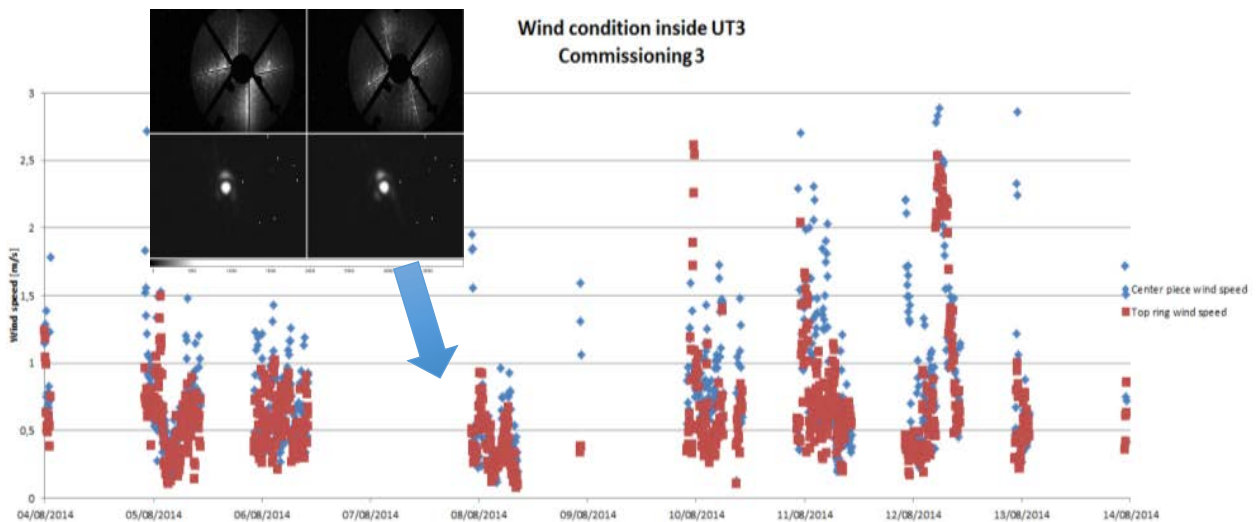


Figure 3 : Wind speed measurement, graduated in meter per seconds during the third commissioning, August 2014. The red squares show the wind speed at the level of top ring (secondary mirror) of UT3. The blue diamonds show the wind speed at the level of the center piece (primary mirror).

The evolution of the LWE on short timescale has been followed by performing images with IRDIS with small Region Of Interest [ROI] and therefore short integration time (DIT=0.06s). At this timescale, no particular nor remarkable time evolution could be seen.

3. UNDERSTANDING THE PHENOMENON

3.1 Large phase discontinuities

A further understanding, as well as a first quantification of the effect have been made when observing the signal of ZELDA wave-front sensor [WFS]. This WFS is composed of a focal-plane phase mask combined with a pupil plane imaging downstream of this mask. The focal plane mask shifts by π a circular central core (of size 1.06 diffraction) with respect to the rest of the focal plane. The interference created by this device allows one to code almost directly the phase as an intensity pattern in the next pupil plane (N'Diaye et al, 2013).

The ZELDA WFS is present on SPHERE instrument and was used during a moderate case of LWE of commissioning 4 (October 2014), producing the phase map of Figure 4 (a). In this phase map, the shadow of the secondary mirror of UT3 (14% in diameter) as well as the shadows of the mechanical spiders are visible. The wave-front also presents the bright spots symptomatic of some of the dead actuators of High Order Deformable Mirror [HODM], at their expected position in the pupil. Some strong discontinuities are visible, between each side of the spider arms. These four arms delimitate four sections of the pupil, in which different local piston, tip and tilt aberrations are present. The highest phase discontinuity is located around the bottom/left spider arm, with almost 800 nm of wave-front step according to the ZELDA measurement.

The phase steps are extremely sharp, finely delimited by the spider arm, as shown on the Figure 4 (b). This figure shows the phase map of Figure 4 (a), but cropped at 1/40th of the pupil, which is the area covered by a sub-aperture of the SAXO WFS. This zoomed display shows that the discontinuity width is clearly narrower than a sub-aperture, hence extremely difficult to measure and to modelize with a 30% coupling influence function of the HODM.

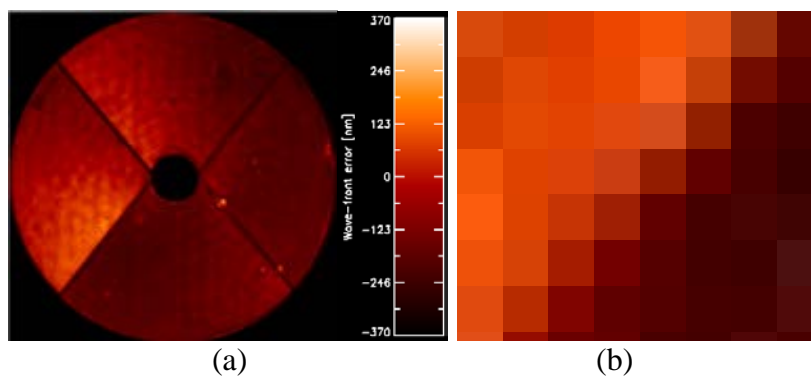


Figure 4: Wave-front aberration measured by ZELDA WFS of SPHERE, during on-sky measurement of commissioning 4. (a) Measurement taken on the whole pupil. (b) Zoom of (a) on an area covered by one subaperture, along the spider arm bottom/left. The aberration presents strong discontinuities up to hundreds of nanometers (optical wave-front).

3.2 Validation of ZELDA measurement

In the presence of such an unusual phase pattern as the LWE, the priority is to validate the measurement made by ZELDA WFS. This validation is proposed here. From the phase aberration \emptyset measured by ZELDA (presented in Figure 4a) and the pupil shape P (a round pupil with 14% central occultation), a PSF h is computed by considering the following relation:

$$h = |\text{TF}(P e^{i\emptyset})|^2 \quad (1)$$

The result of this simulation is shown in the Figure 5. The simulated PSF is shown in (b), and has to be compared (qualitatively) with (c), which is the DTTS image acquired simultaneously with the ZELDA measurement. The PSF are shown in logarithmic scale. The division of the first Airy ring, symptomatic of the LWE is clearly reproduced in the simulation with a good quality. The three main bright Speckles of the first Airy ring are clearly visible, with roughly the correct intensity and size. This validation enforces the LWE pattern measured by ZELDA. It also explains the structure of the degraded PSF seen in (c): the wave-front inclination (tip/tilt) of each of the quadrant of the whole pupil can be seen as creating an independent PSF, each of them centered at a position depending on the tip/tilt value of the corresponding quadrant. Of course the image formation is more complex than that, as the final image formation is issued from a coherent recombination of the electric field coming from the whole pupil. But this approximated (and incoherent) statement explains why there is at maximum four bright Speckles in the LWE PSF, no more than that: there can be only four bright speckles, because there is only four quadrants in the pupil shape.

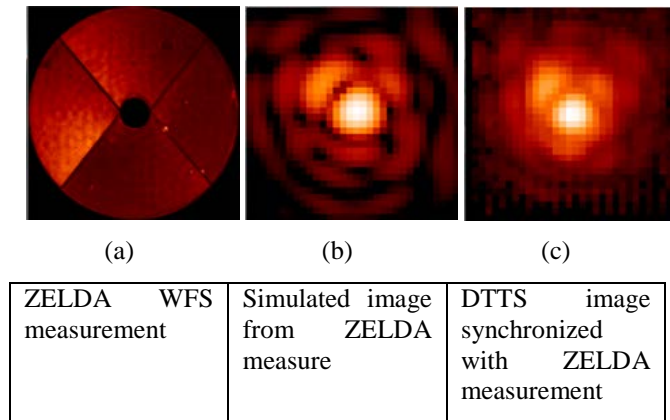


Figure 5: comparison of DTTS image (c) with a PSF (b) simulated by using the ZELDA wave-front measurement (a) and the simple image formation of Equation (1).

4. INSPECTION OF ADAPTIVE OPTICS DATA

The extreme sharpness of the phase steps diagnosed by ZELDA WFS are a first hint that the AO system alone is not able to generate the LWE pattern. The origin of the LWE is therefore situated somewhere else in the optical path. But in order to fully understand the AO system behavior in the presence of LWE, we present here an overview of AO data in the presence of LWE pattern, as measured on-sky.

4.1 High Order Deformable Mirror data

First of all, the deformable mirror data are investigated. A complete set of HODM voltage are acquired at a framerate of 1200Hz on a 30 second period during a strong LWE episode. Some information are shown in the Figure 6. In (a), the ZELDA WFS measurement is shown for remind. In (b), the average of the HODM voltages is shown. This average is obtained by averaging the rough voltage with respect to time, and subtracting the offset voltage (voltage used to flatten the HODM).

$$\bar{v}_k = \langle v_k(t) \rangle_t - \overline{v_k^{\text{offset}}} \quad (2)$$

Thus, the sole static contribution of the internal defects of SPHERE instrument and telescope is shown here. No evidence of the LWE pattern can be found in this map. The Figure 6c shows the variance of each actuator, which is given by the Equation:

$$\sigma_{\text{actuator } k}^2 = \langle |v_k(t) - \bar{v}_k|^2 \rangle_t \quad (3)$$

The Figure 6d e and f show the instantaneous voltage map of HODM, subtracted from the offset voltage. The three instants chosen are 0, 10 and 20 seconds, regularly positioned along the 30 seconds acquisition. No particular step shape can be seen in these snapshots, proof that the HODM is not generating this defect, or that the DM is not the only responsible for the generation of the defect.

$$v_k(t)_{t=[0,10,20] \text{ second}} \quad (4)$$

Again, no particular behavior can be seen at the position of the spider. The highest variance appear

- Close to the outer edge of the pupil, the corresponding sub-apertures are less illuminated than the other and therefore present more noise, conducting to a more oscillating actuator;
- Close to the inner edge of the pupil, for the same reason the actuator situated close to the center are more oscillating than the other;
- Close to dead actuators, the actuators neighbor of a dead actuator are submitted to more stress as a part of the uncorrected phase at the position of the dead actuator can be partially corrected by its neighbor thanks to the coupling factor, at the price of a stronger deformation on the neighbor actuator.

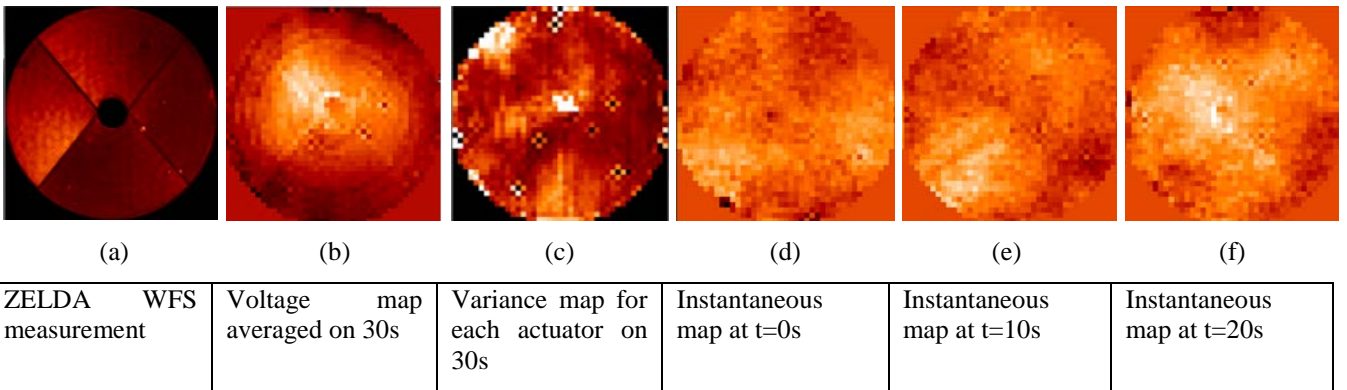


Figure 6: HODM voltage statistics, and comparison to the LWE pattern as seen by ZELDA WFS. From the instantaneous voltage acquisitions (d, e and f) are computed average values (b) and variance (c).

4.2 Wave-front sensing data

The wave-front sensor of SPHERE instrument is a spatially filtered Shack-Hartmann of 40x40 sub-apertures. The measurement of this WFS have been acquired simultaneously with the HODM voltage described in the previous section, and simultaneously with the DTTS image already presented in the previous section.

The slopes are measured at 1200Hz for the 1240 sub-apertures, and recorded during a 30seconds period. From these slopes, the statistical variance is computed as Equation (5), and displayed in the Figure 7a and Figure 7b. In the case of Figure 7a, the LWE was not present. This measurement has been acquired a different night, under different wind conditions. It is only here to witness the nominal situation without LWE.

$$\sigma_{\text{Sub-aperture } k}^2 = \langle |s_k(t) - \bar{s}_k|^2 \rangle_t \quad (5)$$

With $\bar{s}_k = \langle s_k(t) \rangle_t$ being the average slope measured at sub-aperture k .

The Figure 7a shows a uniform variance distribution of the slopes across the pupil. Some higher values can be seen close to the inner edge of the pupil (due to the central occultation). Some slightly higher values can be seen around the visible dead actuators, allowing the fact that the spots in these sub-apertures are less corrected than the others, leading to a higher residual variance.

The Figure 7b shows the variance distribution in the presence of a strong LWE. The main difference with the Figure 7a is the slightly higher variance values of the sub-apertures under the spider arms.

The difference in variance for the sub-apertures situated under the spiders is very faint and does not allow to conclude about the capacity of WFS to fully measure the LWE pattern. But still this residual shows that a difference exists, and the WFS is -at least partially- sensitive to it.

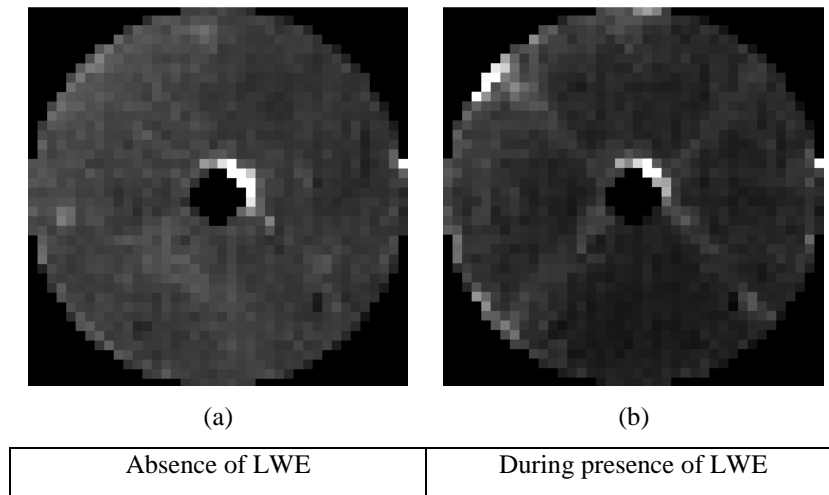


Figure 7: variance map of the residual slopes. The variance is computed according to Equation (5). Two cases are considered, (a) without LWE, (b) during LWE episode.

4.3 LWE and AO system: partial conclusion

Even if the behavior of the SPHERE AO system with respect to LWE is not perfectly understood, the conclusions are:

- LWE is present 20% of the observing time
- LWE is strongly correlated to the wind speed at the level of the telescope
- LWE is composed of strong phase discontinuities, due to apparently independent piston/tip/tilt on each of the four segments of the VLT pupil
- LWE is not generated by HODM
- LWE is partially seen by the WFS

5. PROPOSED SCENARIO FOR LWE EXPLANATION

The scenario that we propose to explain the LWE pattern is based on radiative transfer between the spider and the sky background, decreasing the temperature of the spider by a large amount. The air coming on the spider has therefore a temperature higher than the spider (see Figure 8), and therefore loses heat when crossing the spider. The air after the spider has a decreased temperature T'_{air} . This temperature difference creates a temperature gradient of the air on each side of the spider arm. As an example, a temperature difference of 1° , cumulated on a 1m height, is responsible for an optical path difference of 800nm between each side of the spider.

This scenario has the advantage to explain the following points:

- Such a scenario explains that the optical path difference profile presents a sharp step, the temperature varies very rapidly across the spider
- The OPD created by the air difference will increase when the wind speed decreases.

This scenario is being validated by temperature measurement ongoing on VLT-UT3. The temperature probe will gather large sample of the air and probe temperature around one of the spider arm during observation. These sample will be used to establish a relation between the LWE amplitude as measured by DTTS and the temperature conditions.

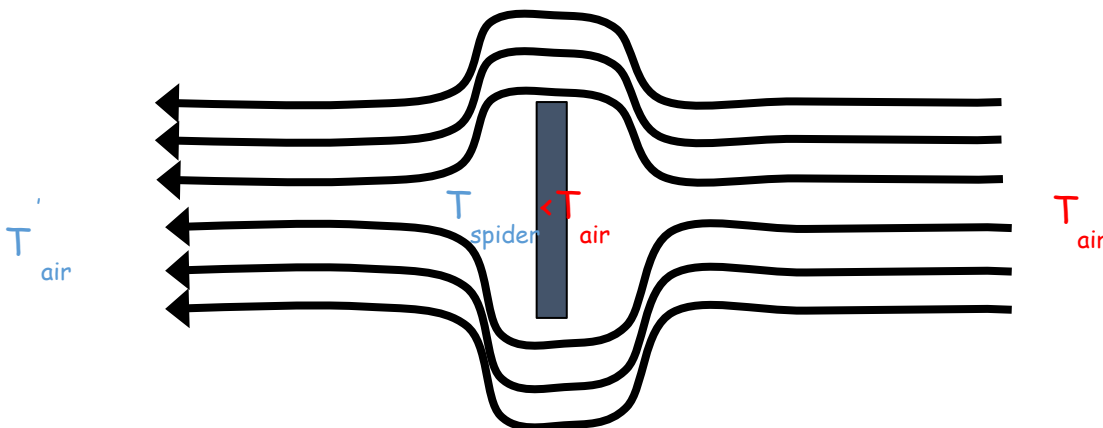


Figure 8: Scenario of the LWE : the radiative transfer decreases the temperature of the spider. Some heat exchange exist between the air at temperature T_{air} and the spider, leading to a difference

6. DEFINITION OF A LWE CRITERION

Even if the conclusions on LWE are only partial up to now, we propose here to define a criterion able to quantify and monitor the LWE during the SPHERE instrument operation. This criterion will be added to the science data, as part of the AO data, enabling to flag the image corrugated by the effect. ZELDA WFS is not a good candidate to perform the monitoring aspect of this criterion, because the ZELDA mask needs to be inserted instead of the coronagraphic mask. This is the reason

why we propose to derive a criterion based on focal-plane phase retrieval from DTTS images. These images are constantly available during operation, and are already often used as a visual warning of the LWE presence.

The Phase Diversity technique is a focal-plane WFS able to retrieve the phase (and amplitude if needed) aberrations from a focal plane information, composed of two images. One focal-plane image, and one out-of-focus image. Typically the out-of-focus value is set to 1.814 radians RMS of Z_4 , this value giving optimal results in some conditions. Two images are required in order to release the sign ambiguity of the phase map. With only one image (acquired in focus), the phase estimation is correct except for the sign of its centrosymmetric contribution.

We only want to develop a criterion able to quantitatively give the amplitude of LWE, but in a monitoring scheme we do not need the exact shape (and sign) of the LWE pattern, the only Peak-to-Valley value is enough to quantify the error. Therefore a simple solution based on a single image phase diversity process is proposed here.

The principle of the phase diversity is to minimize a maximum likelihood criterion $J(\emptyset)$ computed as the norm of the difference between the image and a model of this image. This criterion is classically defined as:

$$J(\emptyset) = \|i - \alpha h(\emptyset)\|^2$$

With i being the acquired image, $\alpha h(\emptyset)$ is the model of the image with α the flux of the source, \emptyset the phase aberrations and $h(\emptyset) = |\text{TF}(Pe^{i\emptyset})|^2$ (same notations than Equation 1). The parameters of the image are therefore the source flux and the phase aberrations. The phase aberrations are usually defined as a combination of N Zernike modes:

$$\emptyset = \emptyset_Z = \sum_{k=1\dots N} a_k Z_k.$$

Here the model of the phase is modified to include the specificity of the LWE pattern. The phase model becomes a sum of the LWE contribution and a low-order contribution:

$$\emptyset = \emptyset_{\text{PTT}} + \emptyset_Z$$

With \emptyset_{PTT} being the LWE contribution which is modeled as a piston tip and tilt contribution on each segment:

$$\emptyset_{\text{PTT}} = \sum_{j=1,4} \sum_{k=1,3} a_{j,k}^{\text{PTT}} P_j Z_{k,j}$$

- P_j is the pupil mask function for the j^{th} quadrant
- $a_{j,k}^{\text{PTT}}$ is the coefficient of the k^{th} Zernike mode for the j^{th} quadrant
- $Z_{k,j}$ is the k^{th} Zernike mode defined on the j^{th} quadrant. In particular this definition implies to guarantee that the tip and tilt modes do not include any piston when defined on the j^{th} quadrant.

The estimation itself is then done by minimizing the criterion with respect to the searched parameters:

$$\{\hat{\alpha}; \hat{a}_{j,k}^{\text{PTT}}; \hat{a}_k\} = \operatorname{argmin} J(\alpha, a_{j,k}^{\text{PTT}}, a_k)$$

6.1 Validation on simulated data

The validation of this estimator is made on simulated data. The model used to simulate the data is the same than the model used during the reconstruction process, except for the noise contribution. 10 Zernike modes are simulated for the low order contribution Φ_Z .

The image simulated with LWE effect is shown in Table 1, top/left. A detector noise representative of the DTTS detector is used, as well a magnitude 9 star and a typical exposure time of 1 second as used by DTTS.

The low order contribution Wave-front error [WFE] is set at 50nm RMS, distributed on 15 Zernike modes (from focus Z_4 to Z_{18}).

The piston tip and tilt coefficients are randomly generated with 150nm RMS for each mode, representative of the LWE as measured on SPHERE.

The phase map for LWE and low order contributions are shown in Table 1, top center and top right. The reconstructed data for each of this quantity is shown in the bottom row of Table 1. Only the phase map with the correct sign is shown for each of the contributors. The reconstruction error for the LWE contribution is estimated at 10nm RMS, while the reconstruction error for the low order mode is estimated at 5nm RMS.

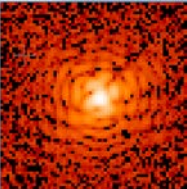
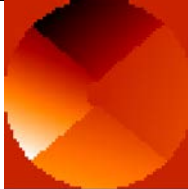
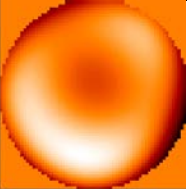
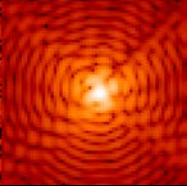
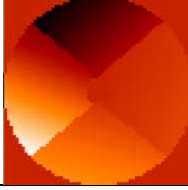
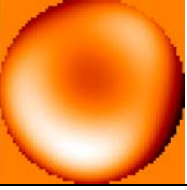
	Image	Φ_{PTT}	Φ_Z
Simulated data			
Reconstructed data			
Reconstruction error [nm RMS]		10	5

Table 1: validation of the LWE estimator on simulated data

6.2 First validation on real data

The estimator is then used on real data. The truth sensor will be ZELDA wave-front sensor. The Table 2 shows the result of the reconstruction of DTTS images. The image is shown on top/left, acquired on-sky in H band during a medium LWE episode. The corresponding wave-front pattern has been measured by ZELDA at the same moment, and is given by

the top/right image. In the bottom/left image, the model of the PSF shows a good concordance with the DTTS image. This is a good health sign of the estimation. The $\hat{a}_{j,k}^{PTT}$ coefficients estimated are used to produce a phase map of the LWE contribution, and shows the correct pattern and amplitude (compared to the ZELDA measurement). Here only the correct sign solution is shown (an opposite sign on the estimated odd part of the phase has been added numerically after the estimation).

This result on experimental data shows that the DTTS image, processed by this simple phase diversity algorithm is an adequate criterion to estimate the LWE amplitude in parallel to the science observation. Some more systematic measurement will be done on all DTTS estimation available from commissioning data, in order to characterize several aspects:

- The domain in which the estimator works correctly and gives a good estimation of LWE (amplitude of LWE, magnitude of guide star...)
- Define a criterion for LWE maximum amplitude before flagging science data
- Define an operational mode for dealing with the LWE once above threshold

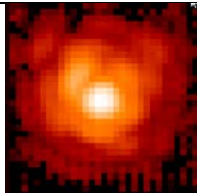
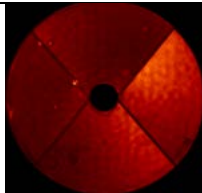
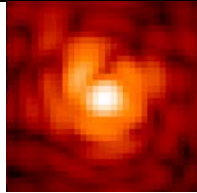
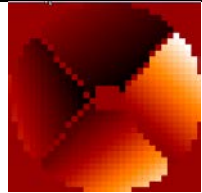
	Image	ϕ_{PTT}
DTTS image / ZELDA measurement		
Reconstructed data		

Table 2: test of the method on real DTTS data, and comparison to ZELDA measurement.

7. CONCLUSION AND PERSPECTIVES

The issue of the Low Wind Effect [LWE] is addressed in this paper. The particular of the origin of this effect has been diagnosed to a dome seeing effect in the telescope, due to heat exchange between the spiders arm and the surrounding air, the spider being at a lower temperature than the air. The impact on the system performance has been diagnosed to several tens of % of Strehl Ratio, with typical signatures representing bright speckles close to optical axis. The particular shape of the effect has reduced interaction with the AO system, a priori due to its spatial frequency content.

The development of a new sensor able to measure the LWE has been demonstrated, this sensor is based on a focal-plane wave-front sensor dedicated to this particular effect. It shows an excellent behavior using the Differential Tip-Tilt sensor [DTTS], this has been confirmed by comparing the measurement to ZELDA measurement.

The issue or the correction of this effect has not been addressed in this paper. Dealing with the LWE as a classical Non-Common Path Aberration [NCPA] could be a solution, at the condition of including the following steps:

- Project the LWE pattern into the slopes space
- Modify the reference slopes accordingly
- Close the loop on modified slopes.

As the defect is apparently badly seen and hardly corrected by the AO loop, this procedure seems to be rather complex to implement.

However, some preliminary tests show that the HODM is able to generate partially a wave-front pattern similar to the LWE, but with reduced spatial frequencies. This introduction has been made through a modification of the reference slopes. Even if this is a very preliminary result, it is very encouraging and is a good hint for solving this problem in the coming year.

8. REFERENCES

- Beuzit, J.-L., Boccaletti, A., Feldt, M., Dohlen, K., Mouillet, D., Puget, P., . . . Baruffolo, A. (2010). *Direct detection of giant extrasolar planets with SPHERE on the VLT* (Vol. Pathways Towards Habitable Planets).
- Fusco, T., Rousset, G., Sauvage, J.-F., Petit, C., Beuzit, J.-L., Dohlen, K., . . . Kasper, M. (2006). *High-order adaptive optics requirements for direct detection of extrasolar planets: Application to the SPHERE instrument*. Optics Express.
- Fusco, T., Sauvage, J.-F., Petit, C., Costille, A., Dohlen, K., Mouillet, D., . . . Soenke, C. (2014). *Final performance and lesson-learned of SAXO, the VLT-SPHERE extreme AO: from early design to on-sky results*. SPIE Astronomical Telescopes+ Instrumentation.
- Mesa, D., Gratton, R., Zurlo, A., Vigan, A., Claudi, R., Alberi, M., . . . Hennin. (2015). *Performance of the VLT Planet Finder SPHERE. II. Data analysis and results for IFS in laboratory*. aap.
- Vigan, A., Bonnefoy, M., Ginski, C., Beust, H., Galicher, R., Janson, M., . . . Salter, G. (2015). *First light of the VLT planet finder SPHERE. I. Detection and characterization of the sub-stellar companion GJ 758 B*. aap.
- Woolf, N. (1979). *Dome seeing*. pasp.
- Zurlo, A., Vigan, A., Mesa, D., Gratton, R., Moutou, C., Langlois, M., . . . Martine. (2014). *Performance of the VLT Planet Finder SPHERE. I. Photometry and astrometry precision with IRDIS and IFS in laboratory*. aap.